The Collection Efficiency of Shielded and Unshielded Precipitation Gauges. Part II: Modeling Particle Trajectories

MATTEO COLLI AND LUCA G. LANZA

Department of Civil, Chemical and Environmental Engineering, University of Genoa, and WMO–CIMO Lead Centre "B.Castelli" on Precipitation Intensity, Genoa, Italy

ROY RASMUSSEN

National Center for Atmospheric Research, Boulder, Colorado

JULIE M. THÉRIAULT

Department of Earth and Atmospheric Sciences, University of Quebec at Montreal, Montreal, Quebec, Canada

(Manuscript received 16 January 2015, in final form 18 June 2015)

ABSTRACT

The use of windshields to reduce the impact of wind on snow measurements is common. This paper investigates the catching performance of shielded and unshielded gauges using numerical simulations. In Part II, the role of the windshield and gauge aerodynamics, as well as the varying flow field due to the turbulence generated by the shield–gauge configuration, in reducing the catch efficiency is investigated. This builds on the computational fluid dynamics results obtained in Part I, where the airflow patterns in the proximity of an unshielded and single Alter shielded Geonor T-200B gauge are obtained using both time-independent [Reynolds-averaged Navier–Stokes (RANS)] and time-dependent [large-eddy simulation (LES)] approaches. A Lagrangian trajectory model is used to track different types of snowflakes (wet and dry snow) and to assess the variation of the resulting gauge catching performance with the wind speed. The collection efficiency obtained with the LES approach is generally lower than the one obtained with the RANS approach. This is because of the impact of the LES-resolved turbulence above the gauge orifice rim. The comparison between the collection efficiency values obtained in case of shielded and unshielded gauge validates the choice of installing a single Alter shield in a windy environment. However, time-dependent simulations show that the propagating turbulent structures produced by the aerodynamic response of the upwind single Alter blades have an impact on the collection efficiency. Comparison with field observations provides the validation background for the model results.

1. Introduction

The goal of this study is to provide numerical estimates of the impact of wind on the catching performance of an unshielded and single Alter (SA) shielded Geonor T-200B vibrating wire gauge. The work is based on a set of underlying three-dimensional airflow fields obtained in Colli et al. (2015a, hereafter Part I) from computational fluid dynamics (CFD) simulations. The modeled shield–gauge geometry is shown in Fig. 1 of Part I. The flow patterns are derived from the solution of the three-dimensional motion equations of the airflow realized around a shielded and unshielded gauge under varied undisturbed wind conditions.

Part I investigated the pattern of streamlines near the shield–gauge configuration using two approaches, namely, the time-invariant method based on the Reynolds-averaged Navier–Stokes (RANS) equations and the time-variant method based on large-eddy simulations (LESs). Both of them provide estimates of the airflow turbulence generated by the shield–gauge assembly within the undisturbed laminar wind field by means of the spatial distribution of the turbulent kinetic energy parameter k. In addition, LES directly solves the large scales of the fluctuating flow and provides time-dependent air velocity and pressure fields (U and p, respectively). This would overcome the limitations of previous numerical studies of the

Corresponding author address: Matteo Colli, Department of Civil, Chemical and Environmental Engineering, University of Genoa, Via Montallegro 1, CAP 16145 Genoa, Italy.
E-mail: matteo.colli@unige.it

DOI: 10.1175/JHM-D-15-0011.1

catching performance of snow gauges, which are focused on time-invariant solutions only and neglect the particle density in the calculation of the resulting collection efficiency (Folland 1988; Nešpor and Sevruk 1999; Thériault et al. 2012).

The RANS simulations showed that the time-averaged wind speed upstream of the gauge is lower when using an SA shielded gauge instead of an unshielded gauge. Higher values of U and k were computed above the collector in an unshielded configuration when compared to the SA shield. The paired RANS simulation and LES highlighted a general underestimation of turbulence by the former model just above the gauge orifice rim. The time-variant analysis clearly showed that propagating turbulent structures generated by the aerodynamic response of the upwind SA blades have a relevant impact on the k fields above the gauge collector (Part I). The actual impact of this on the expected undercatch can only be evaluated after tracking the precipitation particles.

In this paper, we use a Lagrangian tracking model (LTM) to calculate the collection performance of unshielded and SA shielded precipitation gauges. The LTM predicts the snowflake trajectories starting from the underlying airflow fields computed by both RANS simulation and LES. The first part of the analysis follows the methodology proposed by Thériault et al. (2012) to address a comparative evaluation of the catching performance of shielded and unshielded gauges with the RANS time-invariant approach. In a second instance, the impact of time-variant airflows on the trajectories is investigated by means of a modified LTM, based on the LES outputs. This is a novel analysis of the impact of fluctuating air velocity fields onto the trajectory model for the SA shielded gauge.

2. Method

a. Calculation of the collection efficiency

The catching performance of the snow gauges is calculated by running numerical simulations of the trajectories for a number of snowflake types and sizes. This is possible by assuming the particle physical characteristics as described by a general power law (Rasmussen et al. 1999) in the form

$$X(d_p) = a_X d_p^{b_X}, \tag{1}$$

where d_p is the particle diameter and X assumes the nomenclature of the particle terminal velocity w_T, volume V_p, bulk density ρ_p, and cross-sectional area A_p.

For the sake of simplicity, we categorize the hydrometeors as wet and dry snow only. In a second step, we integrate the results over a proper particle size distribution (PSD) for the hydrometeors in order to obtain gauge performance at any given precipitation rate.

TABLE 1. Parameters a_X and b_X of Eq. (1) (Rasmussen et al. 1999) for the computation of the snowflake terminal velocity (i.e., w_T), volume (i.e., V_p), bulk density (i.e., ρ_p), and cross-sectional area (i.e., A_p).

	a_{w_T}	b_{w_T}	a_{V_p}	b_{V_p}	a_{ρ_p}	b_{ρ_p}	a_{A_p}	b_{A_p}
Dry snow	107	0.2	$\pi/6$	3	0.017	−1	$\pi/4$	2
Wet snow	214	0.2	$\pi/6$	3	0.072	−1	$\pi/4$	2

The values of the parameters a_X and b_X are provided in Table 1. This parameterization was employed by Thériault et al. (2012) for the LTM simulations, obtaining a good agreement between the modeled and in-field observations at the Marshall test site, Colorado, with data properly classified by crystal types using a photographic technique.

Although modifications are necessary to study the effect of time-variant flow fields and to improve the calculation of the gauges' undercatch in mass-weighted terms, the LTM follows Nešpor and Sevruk (1999) and Thériault et al. (2012). The tracking algorithm is based on the equation of motion

$$V_p \rho_p \mathbf{a}_p = -\frac{1}{2} C_D A_p \rho_a (\mathbf{v}_p - \mathbf{v}_a)|\mathbf{v}_p - \mathbf{v}_a| + V_p(\rho_p - \rho_a)\mathbf{g}, \tag{2}$$

where $\mathbf{a}_p$ is the snowflake acceleration, $\mathbf{g}$ is the gravity acceleration, C_D is the drag coefficient, V_p is the particle volume, A_p is the cross sectional area, and ρ_a and ρ_p are the density of the air and the snow particles. Solving Eq. (2) for the particle-to-air magnitude of velocity vector, we obtain

$$|\mathbf{v}_p - \mathbf{v}_a| = [(u_p - u_a)^2 + (v_p - v_a)^2 + (w_p - w_a)^2]^{1/2}, \tag{3}$$

where u, v, and w represent the streamwise, crosswise, and vertical components of velocity. The three components of the particle acceleration from Eq. (2) are

$$a_{p_x} = -\frac{1}{2} C_D A_p \frac{\rho_a}{V_p \rho_p}(u_p - u_a)|\mathbf{v}_p - \mathbf{v}_a|, \tag{4a}$$

$$a_{p_y} = -\frac{1}{2} C_D A_p \frac{\rho_a}{V_p \rho_p}(v_p - v_a)|\mathbf{v}_p - \mathbf{v}_a|, \quad \text{and} \tag{4b}$$

$$a_{p_z} = -\frac{1}{2} C_D A_p \frac{\rho_a}{V_p \rho_p}(w_p - w_a)|\mathbf{v}_p - \mathbf{v}_a| + \frac{(\rho_p - \rho_a)}{\rho_p} g, \tag{4c}$$

where the x, y, and z subscripts mark the streamwise, crosswise, and vertical components of particle acceleration and the third equation has an additional term g to consider the gravity force in the vertical particle

acceleration. While the drag coefficient of a falling particle is influenced by the instantaneous particle-to-air magnitude of velocity through the particle Reynolds number (Stout et al. 1995; Nešpor and Sevruk 1999), the present methodology adopts the simplification of using a fixed C_D during the particle motion calculated as a function of the particle terminal velocity given as

$$C_D = \frac{2V_p(\rho_p - \rho_a)g}{A_p \rho_a w_T^2}. \tag{5}$$

The influence of turbulence on the particle drag is ignored in this formulation. Although this formulation would be exact in the case of stagnant air, we are neglecting the bond between turbulence and the particle drag (the drag curve). The work of Thériault et al. (2012) demonstrated that this hypothesis does not lead to relevant inaccuracies. Considering that the volume and the density of the snowflakes are a function of d_p, following Eq. (1) we obtain the C_D formulation as

$$C_D = \frac{2g a_{V_p} a_{\rho_p}}{a_{A_p} \rho_a a_{w_T}} d_p^{(b_{V_p} + b_{\rho_p} - b_{A_p} - 2b_{w_T})}. \tag{6}$$

Thériault et al. (2012) report on the theoretical C_D curves as a function of d_p for various types of snowflake crystals using the Rasmussen parameterization (Rasmussen et al. 1999) and including dry and wet snow as reported in Table 1. Equation (6) shows a general decrease of the particle drag with increasing diameter; the inertial forces of the larger particles dominate the viscous effects with trajectories that are theoretically less conditioned by the airflow conditions. The trajectories are therefore easily computed with a forward steps procedure for a given snowflake type, d_p, and free-stream velocity U_w by calculating at short time intervals Δt the variations of the particle position until the trajectory remains in the proximity of the gauge. This is achieved by the following set of equations:

$$\Delta x = x_2 - x_1 = \left(u_{p_1} + \frac{1}{2} a_x \Delta t\right)\Delta t, \tag{7a}$$

$$\Delta y = y_2 - y_1 = \left(v_{p_1} + \frac{1}{2} a_y \Delta t\right)\Delta t, \quad \text{and} \tag{7b}$$

$$\Delta z = z_2 - z_1 = \left(w_{p_1} + \frac{1}{2} a_z \Delta t\right)\Delta t, \tag{7c}$$

where x_1, y_1, and z_1 and x_2, y_2, and z_2 are, respectively, the previous and the new spatial coordinates of the particle. The velocity components assigned to the new particle position (u_{p_2}, v_{p_2}, and w_{p_2}) are updated by adding the following increments to the previous step values:

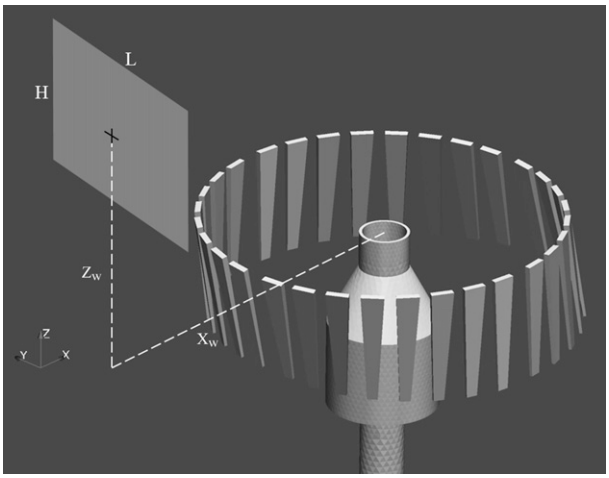

FIG. 1. Positioning of the seeding window (product of length L and height H) at a fixed streamwise distance x_w upstream of the gauge orifice and variable elevation z_w with respect to the collector.

$$\Delta u_p = u_{p_2} - u_{p_1} = a_x \Delta t, \tag{8a}$$

$$\Delta v_p = v_{p_2} - v_{p_1} = a_y \Delta t, \quad \text{and} \tag{8b}$$

$$\Delta w_p = w_{p_2} - w_{p_1} = a_z \Delta t. \tag{8c}$$

Note that from Eq. (4) the acceleration vector $\mathbf{a}_i$ at the ith time step is dependent on the particle-to-air velocity difference $\mathbf{v}_p - \mathbf{v}_a$, meaning that an interpolation scheme of the air velocity gridded values to the exact $\mathbf{x}_i$ has to be applied. This is acceptable considering the high spatial resolution of the mesh in the vicinity of the windshield and the gauge bodies, where the velocity gradients are larger. The Lagrangian procedure does not handle the collisions between particles since trajectories are solved independently from each other.

To reduce the computational burden of the simulation, only a reduced number of trajectories within the spatial domain are simulated. The choice of the initial particle locations determines the simulated trajectories. The initial positions of the simulated trajectories lay on an ideal vertical plane located upwind of the windshield and the orifice level. Figure 1 shows the selected seeding window and its location relative to the shield–gauge assembly. The seeding window is oriented crosswise to the undisturbed wind field, at a fixed distance upstream of the gauge, but with variable elevation with respect to the collector as a function of the wind velocity, the crystal type, and the particle diameter.

To calculate the wind-induced undercatch, we assume, as in Thériault et al. (2012), an inverse exponential PSD of the hydrometeors in the form

$$N(d_p) = N_0 \exp(-\Lambda d_p), \tag{9}$$

where N_0 ($\mathrm{mm^{-1}\,m^{-3}}$) is the intercept parameter, Λ ($\mathrm{mm^{-1}}$) is the slope, and d_p is the particle diameter. Nešpor (1995) defined the gauge catching performance for a specific d_p/U_w combination as the catch ratio r (unitless), here defined as

$$r = \frac{A_{\text{inside}}(d_p, U_w)}{A_{\text{gauge}}}, \tag{10}$$

where $A_{\text{inside}}(d_p, U_w)$ is the effective collecting area associated with the number of particles collected by the gauge and $A_{\text{gauge}}(d_p, U_w)$ is the area associated with the entering particles in case of undisturbed airflow.

The catching performance of the snow gauges are here quantified by the collection efficiency (CE) variable. We estimate CE starting from a particle counting technique as in Thériault et al. (2012), with an integral formulation expressed as

$$\mathrm{CE}(U_w) = \frac{\int_0^{d_{p\max}} A_{\text{inside}}(d_p, U_w) N(d_p) d_p}{\int_0^{d_{p\max}} A_{\text{gauge}} N(d_p) d_p}. \tag{11}$$

However, the investigated gauge actually measures the equivalent depth (or volume) of precipitation by weighing the water entering the orifice area. To ensure that theoretical results can be compared with in-field estimates of the collection efficiency, it was assumed that the density of snow varies with d_p, yielding

$$\mathrm{CE}(U_w) = \frac{\int_0^{d_{p\max}} V_w(d_p) A_{\text{inside}}(d_p, U_w) N(d_p) d_p}{\int_0^{d_{p\max}} V_w(d_p) A_{\text{gauge}} N(d_p) d_p}, \tag{12}$$

with $V_w(d_p)$ denoting the equivalent water volume.

The new (mass weighed) formulation for the collection efficiency, here called the volumetric method, highlights a double dependency of CE on the particle diameter through their volume and the density as well. That is, we account for the actual volume of the collected precipitation in CE, the analysis being now consistent with the formulation provided in terms of precipitation rate by Nešpor and Sevruk (1999) and the in-field measurements, expressed with the usual volumetric per unit area dimensions.

b. Experimental design

The trajectory model is run initially with the underlying RANS airflow in the shielded and unshielded configurations. The model is initialized with the air velocity vectors obtained from the CFD results without accounting for the simulated turbulent kinetic energy fields. Therefore, our time-averaged approach only considers turbulence in averaged terms, that is, insofar as it affects the mean airflow. Multiple runs are produced for a set of 10 wind speeds (U_w = 1–10 $\mathrm{m\,s^{-1}}$) and two different crystal types (representative of wet and dry snow) as in Thériault et al. (2012). The trajectory results provide the necessary information to compute the CE(U_w) curve using the volumetric integration method [Eq. (12)].

The time-dependent approach is different and is computationally heavier. The velocity vectors are indeed refreshed, using the LES outputs at every 0.05 s. Multiple LES were produced for the SA shielded Geonor. Eight wind speeds (U_w = 1–8 $\mathrm{m\,s^{-1}}$) were simulated at 1 $\mathrm{m\,s^{-1}}$ increments, for both wet and dry snow.

In the time-dependent configuration, we estimated the overall CE over the total time by repeating the trajectories' computation with six starting times, which employed different initial airflow configurations. The use of the particle tracking algorithm within a time-dependent approach required implementation of a refined version of the LTM. The time-dependent LTM provides six sets of trajectories yielding six collection efficiency values (based on the volumetric integration method) for each tested wind speed and crystal type. The resulting CE curves derive from the average values of these six runs at each wind speed, while their dispersion provides an indication of the time dependency of the problem.

3. Results and discussion

a. Comparison of shielded and unshielded time-averaged results

We initially considered a set of trajectories based on the time-invariant airflow fields for the unshielded and the SA shielded gauge configurations. The resulting dataset includes multiple simulations for varying undisturbed wind speed, particle diameter, and crystal type.

Figure 2 reports a selection of the dry snow crystal trajectories (with d_p = 5 mm) for both a shielded (Fig. 2, left) and unshielded (Fig. 2, right) configuration. The rows show various undisturbed wind regimes (from 2 to 4 $\mathrm{m\,s^{-1}}$ from top to bottom). Particles are released from the vertical seeding window (see Fig. 1) upwind of the gauge on the left-hand side.

In Fig. 2 (top left), the spacing of the trajectories entering from the left side—to be viewed as constant under undisturbed wind conditions—shows zones of concentration and dilatation. Snowflakes tend to concentrate or disperse their wind-driven trajectories in certain regions,

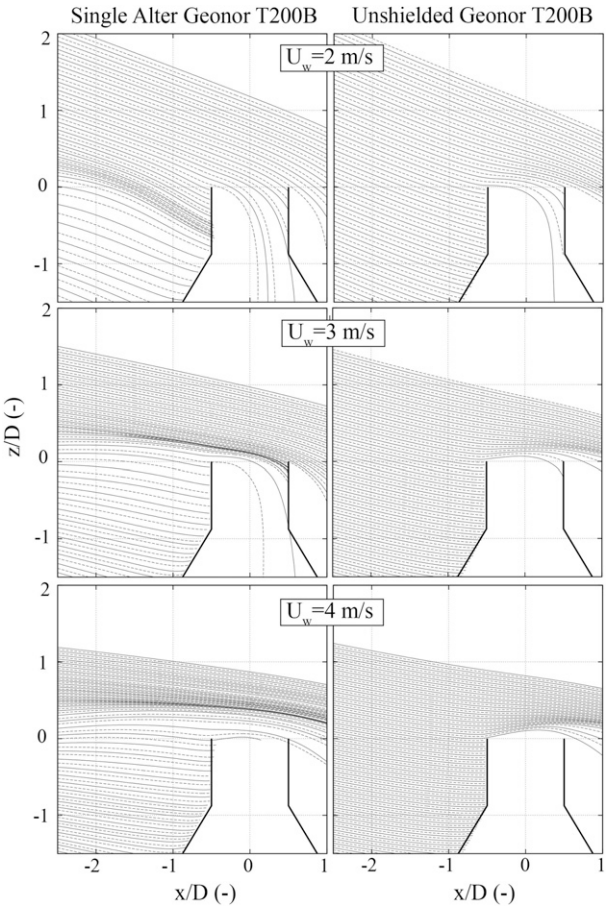

FIG. 2. Deformation of the dry snowflake trajectories near the (left) SA shielded and (right) unshielded gauge with increasing wind speed (time-independent RANS airflows with $d_p = 5\,\text{mm}$). The seeding window of the trajectories is located upstream of the windshield at a nondimensional streamwise distance equal to $x/D = -6.25$.

depending on the local configuration of the air velocity field. As described in Part I, significant local air velocity gradients and strong updrafts occur in the region between the upstream shield blades and the gauge collector. The updraft is strong enough to shift the particle trajectories upward, while the free space above the shield–gauge configuration shows a relevant horizontal air velocity. When trajectories that are shifted upward reach this zone, the upper-level airflow blocks any further lifting of the particles, causing an accumulation of trajectories at the level of the orifice. For this reason, the observed concentration and dispersion of trajectories (a feature called here the clustering effect) is caused by the combined windshield and gauge aerodynamic influence on the particle falling paths and may play a relevant role on the catch performance, depending on the wind speed. Figure 2 (left) highlights this phenomenon and shows that the particle cluster is dragged upward with increasing wind speed (and the associated updraft). At low wind speed, the trajectories passing above the SA shield remain mainly undisturbed until close to the gauge orifice, with a high number of particles falling inside the gauge. At $3\,\text{m s}^{-1}$, the cluster of trajectories is deflected upward and a convergence zone occurs at the level of the gauge collector, leading to a larger number of entering particles than at $2\,\text{m s}^{-1}$. At $4\,\text{m s}^{-1}$ the number of collected particles is drastically reduced, because of the cluster shifting upward, far from the gauge orifice, as a result of stronger vertical velocities on the upstream side of the orifice. A different scenario is reported for the unshielded Geonor T-200B (Fig. 2, right) where the snow trajectories are solely deflected by the action of the gauge orifice. In this case, the number of trajectories that cross the gauge collector gradually decreases by increasing the U_w.

A first estimate of the gauge collection capabilities under the various RANS testing conditions is obtained by simply counting the entering particles with respect to the expected number in case of an undisturbed velocity field. Figure 3 shows the catch ratios for each snowflake diameter, providing a first estimate of the actual contribution of different particle sizes to the total CE in the case of a shielded gauge and dry snow. The gauge undercatch is more evident for the lighter particles.

The lowest wind regime ($U_w = 1\,\text{m s}^{-1}$) shows a flat catch ratio distribution for the shielded gauge (Fig. 3a) over the particle diameter with values varying from 0.9 to 0.95. At an intermediate wind speed ($U_w = 4\,\text{m s}^{-1}$), particles smaller than $d_p = 4\,\text{mm}$ missed the gauge completely. Only at the largest diameter is r comparable with the values observed under weak wind regimes. Finally, a severe wind speed simulation ($U_w = 8\,\text{m s}^{-1}$) confirms this trend with null r values across the whole PSD.

Looking at the dry snow catch ratio for the unshielded configuration (Fig. 3b), among the three represented U_w conditions, only the lowest one ($U_w = 1\,\text{m s}^{-1}$) resulted in r distributions that contain particles of all diameters.

The total CE(U_w) [Eq. (12)] of the unshielded and shielded gauge is shown in Fig. 4. Large variations in the collection efficiency are present in the SA case when compared to the unshielded gauge. For example, the collection efficiency of dry snow increases at $U_w = 3\,\text{m s}^{-1}$ (CE = 95%) followed by the rapid decrease to a zero collection efficiency at $5\,\text{m s}^{-1}$. This sharp variation is explained by the clustering effect highlighted in Fig. 2. This is supported by the size distribution of dry snow falling in the gauge shown in Fig. 3. For the wet snowflakes (triangle symbols), the collection efficiency decreases gradually with increasing wind speed without reaching zero. The wet and dry snow CE associated with the unshielded gauge (gray lines) is generally less than the shielded gauge. Note that, at the highest wind regime ($U_w \geq 9\,\text{m s}^{-1}$), the collection efficiency is higher for the unshielded gauge.

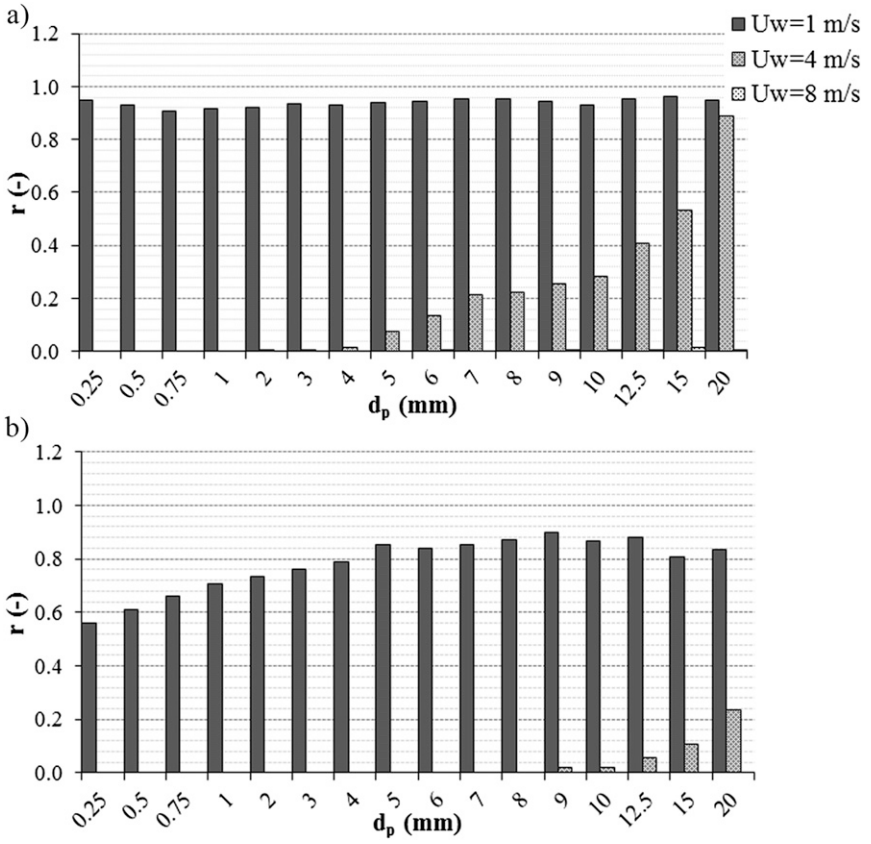

FIG. 3. Dry snow catch ratio (unitless) vs the particle diameter (mm) at three wind speeds ($m\,s^{-1}$) for the (a) SA shielded and (b) unshielded gauge based on the time-averaged (RANS) approach.

Overall, for wet snow, the CE decreases nearly linearly between 1 and $8\,m\,s^{-1}$ for the unshielded gauge. At $U_w > 8\,m\,s^{-1}$, the CE remains constant at ≈ 0.3. This requires further investigation based on a wider spectrum of d_p and crystal types under severe wind regimes. Experimental observations in the field confirm such behavior (Colli 2014).

b. *The influence of time-variant airflow patterns on the collection efficiency*

This section presents the analysis of the impact of turbulence on the collection efficiency of an SA shielded gauge. The work does not address the turbulence of the incoming airflow and that generated by the rough ground at the lower boundary, which will be the subject of future work. As an initial attempt to include time dependency in the numerical modeling of the CE, this work focuses on the wind-driven turbulence generated by the laminar flow interacting with the windshield and the gauge geometry.

We computed various time-dependent trajectories by varying the starting time t_0 (s) of the particles within the fluctuating flow field. The intertime period between different runs of the LTM was determined for each wind speed according to the characteristic time of the turbulent structures generated by the shield–gauge bodies (Colli 2014). At $2\,m\,s^{-1}$ the resulting intertime value is equal to 0.03 s. For example, six realizations of the

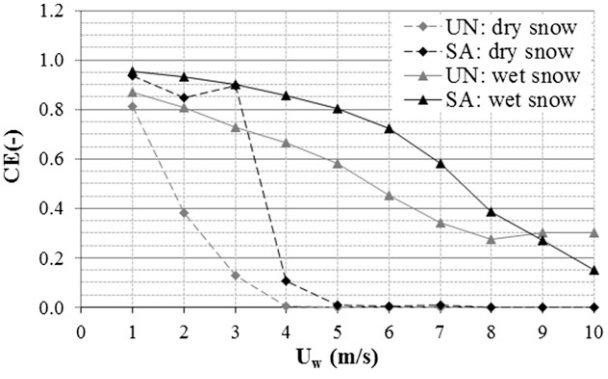

FIG. 4. Dry (diamonds) and wet (triangles) snow CE (unitless) vs wind speed ($m\,s^{-1}$) for the SA shielded (black lines) and unshielded (gray lines) gauge based on the time-averaged (RANS) approach.

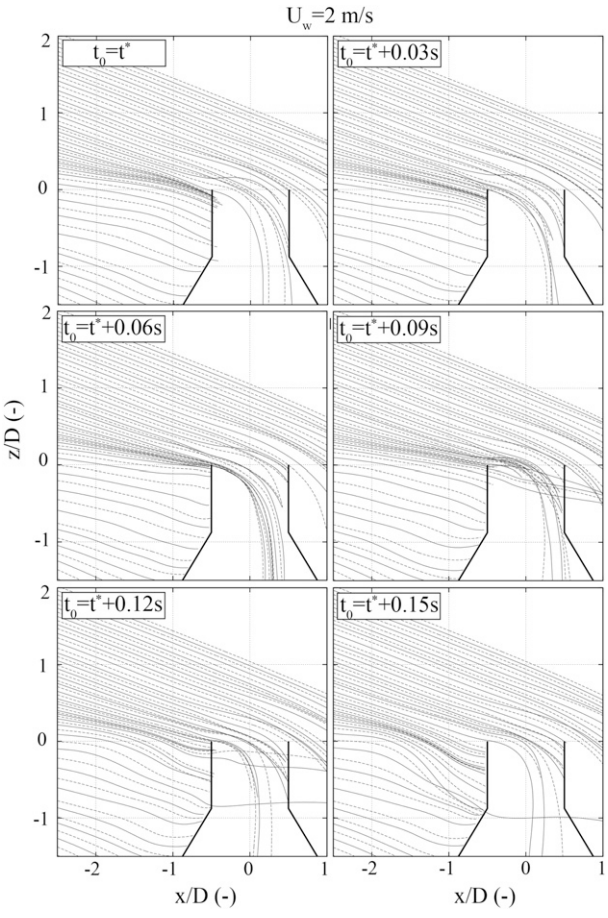

FIG. 5. Streamwise views of the dry snowflake trajectories computed with different starting times (s) with respect to the evolving flow (intertime period equal to 0.03 s). The LTM was run with the following setup: SA shielded Geonor T-200B, $U_w = 2\,\mathrm{m\,s^{-1}}$, $d_p = 5\,\mathrm{mm}$, and LES airflow model.

trajectories computed by the time-dependent LTM are shown in Fig. 5 for dry particles of 5-mm diameter at $U_w = 2\,\mathrm{m\,s^{-1}}$. The irregular distribution of the displayed trajectories results from the turbulent structure of the airflow created by the shield–gauge assembly. These irregular paths are particularly evident in case of dry snow, where trajectories are strongly affected by the air velocity and pressure gradients generated by the upwind shield blades. The wet snow case shows a less complex pattern of trajectories in the space between the windshield and the gauge, thanks to the longer relaxation time of this type of snowflake (Colli 2014).

Table 2 summarizes the influence of the airflow configuration at the beginning of the trajectories' computation on the evolution of the particles paths. Six collection efficiency values CE(t_0) are averaged to account for six different LTM starting times per each tested wind speed and crystal type. The standard deviation σ and coefficient of variation $\mathrm{CV} = \sigma/\mu$ of CE (where μ is the mean) quantify the variability of the catching performance due to the arbitrary choice of the initial configuration of the evolving airflow operated by the LTM.

The dry snow case presents a larger variability of the CE in the $2 \le U_w \le 5\,\mathrm{m\,s^{-1}}$ range. This is confirmed by the values of CV reported in Table 2 that are equal to 0.51 with $U_w = 3\,\mathrm{m\,s^{-1}}$ and 0.85 when $U_w = 4\,\mathrm{m\,s^{-1}}$. At the higher wind speed, the significance of CV decreases because μ(CE) is close or equal to zero [refer to σ(CE)]. This is explained by considering the distribution of the air velocity time series measured near the gauge orifice by Part I. Both the horizontal and the vertical air velocity components revealed a noticeable increase of the amplitude of the fluctuations when moving from $U_w = 2$ to $3\,\mathrm{m\,s^{-1}}$. This enhances the influence of the airflow turbulence on the snowflake trajectories and the associated standard deviation of CE(t_0).

The dispersion of the wet snow CE(t_0) values with U_w shows a different behavior, with a CV(CE) from 0.05 to 0.23 when moving from $U_w = 4$ to $5\,\mathrm{m\,s^{-1}}$ and an increase of CV when $U_w \ge 5\,\mathrm{m\,s^{-1}}$. This is indicative of the fact that the wet, heavier particles require stronger wind regimes to produce the same CE(t_0) variability shown for lower air velocities with dry snow.

By averaging the six $r(t_0)$ values, we obtain the catch ratio histograms reported in Fig. 6 (which is directly comparable with Fig. 3). When $U_w = 1\,\mathrm{m\,s^{-1}}$ (dark gray bars) the gauge collects a larger number of small dry particles. This is a consequence of the convergence of trajectories occurring in the time-dependent implementation of the model. Additionally, the dry snow case presents nonzero values of r over the whole d_p range at an intermediate wind speed equal to $4\,\mathrm{m\,s^{-1}}$, even if the population of large-size collected particles is smaller. Under the strongest wind speed ($U_w = 8\,\mathrm{m\,s^{-1}}$), the gauge collected no dry snow.

Figure 7 illustrates the time-dependent collection efficiency curve $\mu(\mathrm{CE_{DRY}})$ for dry snow (black diamonds) calculated by employing the volumetric method. The $\mu(\mathrm{CE_{DRY}})$ values show again a rapid decrease between $U_w = 2$ and $3\,\mathrm{m\,s^{-1}}$, similarly to what is observed for the time-averaged results between $U_w = 3$ and $4\,\mathrm{m\,s^{-1}}$ (Fig. 2). The gray bars in the background represent the differences (ΔCE) with respect to the time-averaged solution (gray triangles). The main distinction is observed at $U_w = 3\,\mathrm{m\,s^{-1}}$, where the time-averaged CE is influenced by the convergence of trajectories crossing the gauge collectors. Since the clusters of trajectories originate because of the shield aerodynamics, it must be noted that the results presented in this work are representative of the specific SA gauge geometry.

In Fig. 8, the difference between wet snow $\mathrm{CE_{RANS}}$ and $\mathrm{CE_{LES}}$ never exceeds $\Delta\mathrm{CE} = 0.12$, with a good

TABLE 2. Time average (i.e., μ), std dev (i.e., σ), and coefficient of variation (CV) of CE (unitless) computed by varying the trajectory starting time for the wet and dry snow crystal cases.

	U_w							
	1 m s^{-1}	2 m s^{-1}	3 m s^{-1}	4 m s^{-1}	5 m s^{-1}	6 m s^{-1}	7 m s^{-1}	8 m s^{-1}
$\mu(CE_{dry})$	0.85	0.96	0.33	0.15	0.07	0.01	0.01	0.01
$\sigma(CE_{dry})$	0.02	0.08	0.17	0.13	0.05	0.00	0.00	0.01
$CV(CE_{dry})$	0.03	0.08	0.51	0.85	0.72	0.40	0.52	1.33
$\mu(CE_{wet})$	0.89	0.91	0.88	0.83	0.78	0.66	0.46	0.33
$\sigma(CE_{wet})$	0.01	0.01	0.05	0.04	0.18	0.18	0.13	0.16
$CV(CE_{wet})$	0.01	0.01	0.06	0.05	0.23	0.27	0.28	0.49

agreement between the two numerical approaches being observed from 2 to 5 m s^{-1} owing to the slower response time of the wet snow particles. The choice of using a time-independent or time-dependent approach does not affect much the estimation of the total CE for heavier precipitation particles such as wet snowflakes.

c. *Comparison with field observations*

To evaluate the reliability of the current numerical results, we compared our estimates of the CE with observations from the Haukeliseter field site (Norway). Snowfall measurements were made by Wolff et al. (2015) using SA shielded and unshielded Geonor gauges and were compared to the Double Fence Intercomparison Reference (DFIR; Yang et al. 1999; Yang 2014). The recent results of Yang (2014) improved the DFIR estimate of the true snowfall (given by Tretyakov gauge measurements made in bush fences) using Valdai data (Russia) from 1991 to 2010 and provided updated h_{bush}/h_{DFIR} versus U_w curves and regressions (where h represents equivalent water precipitation amount). These equations were used to adjust the DFIR measurements from the Haukeliseter site to improve the estimation of the CE values for two collocated SA shielded gauges. Application of the experimental curves provided by Yang (2014) to different field sites is not rigorous since the local climatology of Valdai has some impacts on the crystals' composition of the snow. However, in general terms, the reduction of the uncertainties related to the DFIR exposure effect leads to in-field CE estimates that are closer to the theoretical formulation.

Figure 9 presents in-field 1-h collection efficiency values for an SA shielded Geonor based on two environmental temperature ranges, $0° > T > -4°C$ (gray dots) and $T < -4°C$ (black dots), respectively. Light precipitation events characterized by an accumulation lower than 0.1 mm have not been included. The two averaged CE curves obtained with time-dependent simulations for wet and dry snow appear in the same plot, together with the box plot distribution of CE values. The wet snow CE curve provides a center to the $T > -4°C$ solid precipitation observations, which is a reasonable result. In this case, the dispersion of the CE values around their mean due to the airflow turbulence seems to explain part of the scatter in the field observations.

The dry snow CE curve provides a lower limit for the set of field data having $T < -4°C$. This is somewhat unexpected, as the dry snow curve should be intuitively

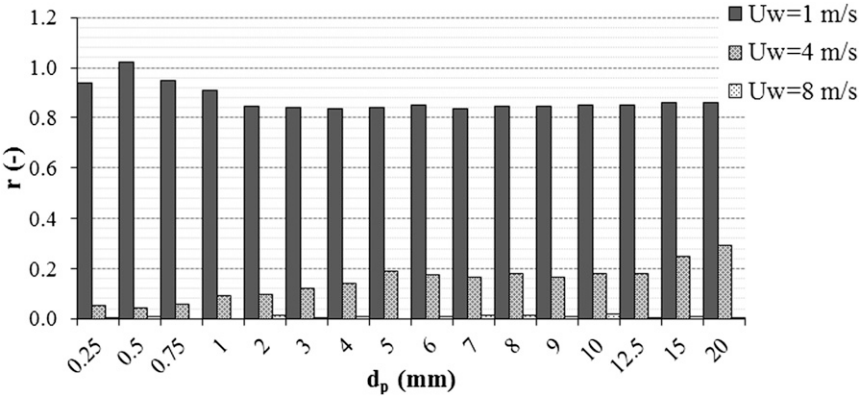

FIG. 6. Dry snow catch ratio (unitless) vs particles diameter (mm) and wind speed (m s^{-1}) for the SA shielded gauge based on the time-dependent (LES) approach.

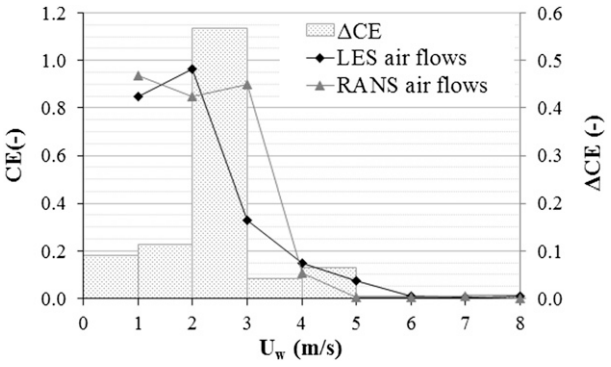

FIG. 7. Dry snow CE (unitless) vs wind speed ($m\,s^{-1}$) for the SA shielded gauge based on the time-averaged RANS and the time-dependent LES approach (gray and black curves, respectively) and their differences (background histograms).

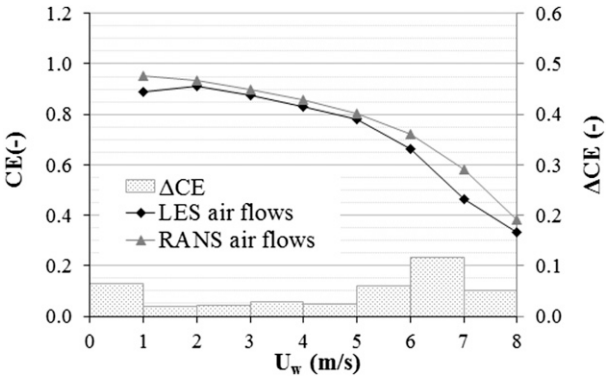

FIG. 8. Wet snow CE (unitless) vs wind speed ($m\,s^{-1}$) for the SA shielded gauge based on the time-averaged RANS and the time-dependent LES approach (gray and black curves, respectively) and their differences (background histograms).

centered on the cold temperature data. It seems that the simulated snow trajectories either have a lower-than-observed terminal velocity leading to a lower CE, or other factors are in play. These could be in-stream turbulence of the airflow, or the fact that the windshield slats are here assumed as stationary while in reality they are free to swivel. The trend in CE is correct, however, showing that simulation captures some of the basic interactions of the snowflakes with the shield–gauge geometry.

In addition, the CE(U_w) curves presented in this section demonstrated a high sensitivity of the particle trajectories to the physical parameterization of the crystal types (see the recurrent comparison between dry and wet snow). Thériault et al. (2012) showed a relevant modulation of the CE curves due to the various snow crystal structures parameterized with the Rasmussen et al. (1999) experimental formulation. Note that the real-world solid precipitation can occur with a blending of different crystal types (further to the possible occurrence of mixed liquid and solid precipitation). In addition, Colli et al. (2015b) reported that the assumption of different drag coefficient formulations for the dry snow particles may impact the trajectories' model results.

On the other hand, various effects related to the airflow can affect the consistency of the comparison between experimental and modeled CE estimates. For example, the contribution of the wind speed variability over the sampling time of the snow measurements can lead to some deviations because the variation of the collection with wind speed is highly nonlinear. This issue can be easily overcome by assuming a maximum value for the coefficient of variation of U_w, as already done for the observations reported in Fig. 9 [CV(U_w) < 0.2].

The use of a static spatial grid for the airflow simulations is another restriction that may influence the resulting airflow and the modeled CE curves. This choice was because, even if the real windshield blades are free to oscillate along the mounting ring when the wind blows, the computational power required to perform an LES analysis over a dynamic mesh is still too onerous (while it may be feasible in the case of time-independent RANS airflow modeling). It is therefore reasonable to attribute part of the in-field data scattering to the crystal type detection issue. This notwithstanding, residual differences between experimental and simulated CE values persist, which are partly attributable to the approximated modeling of the shield–gauge geometries and simplifications of the snowflake characteristics and the tracking scheme.

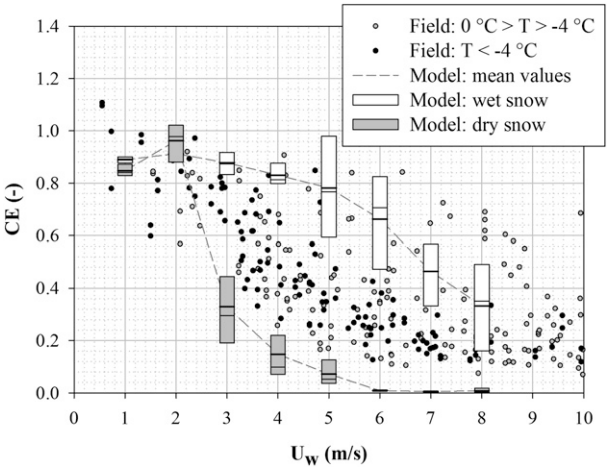

FIG. 9. Comparison between in-field SA shielded (gray and black dots) and modeled (dashed curves with box plots) CE (unitless) vs the undisturbed horizontal wind speed ($m\,s^{-1}$). Field data are classified based on the environmental temperature separating precipitation occurring under $0° > T > -4°C$ from $T < -4°C$.

4. Conclusions

We conducted a numerical modeling analysis of the wind-induced undercatch of snow precipitation gauges. The investigation focused on the weighing-type gauges since they are widely employed for ground-based observations. We calculated snowflake trajectories by using 3D air velocity fields around an unshielded and SA shielded Geonor T-200B vibrating wire gauge under different wind conditions.

The wind fields derive from Part I, where we performed a detailed CFD study of the airflow patterns past shielded and unshielded gauges. Both time-independent (RANS) and time-dependent (LES) models were developed to investigate the role of turbulence generated by the shield–gauge geometry on the deformation of the snowflake trajectories.

The time-independent comparison between CE results obtained by modeling shielded and unshielded gauges validates the empirical choice of installing an SA shield to improve snow measurements. The LES approach revealed the significant time variability of the flow. We used a Lagrangian approach to compute the particle trajectories, assuming no impact of the hydrometeors on the flow and disregarding the possibility of collisions, coalescences, and breakups between the falling particles. The use of a mass-weighted CE formulation accounted for the actual volume of the collected precipitation instead of simply counting the number of particles entering the gauge as in previous literature.

The comparison between RANS and LES airflows highlighted a general underestimation of the turbulence just above the gauge orifice rim by the former model, here parameterized by the turbulent kinetic energy k. As a result, the CE from the LES approach was lower than that derived from the RANS model. The time-dependent simulations showed that the propagation of the turbulent structures, produced by the aerodynamic response of the upwind SA blades, has an impact on the turbulent kinetic energy realized above the gauge collector. This in turn affects the particle trajectories.

The time-dependent CE estimates provided in this work are appreciably lower than existing numerical simulation results obtained by using RANS models (Nešpor and Sevruk 1999; Thériault et al. 2012). This revealed that the turbulence generated by the shield–gauge has an impact on the CE. Multiple runs of the trajectories' computation by starting the snowflake tracking at different instants of the evolving LES airflow demonstrated the influence of turbulence on the particle paths. The noticeable difference between the CE for dry and wet snow crystals demonstrates the importance of the physical parameterization of hydrometeors (terminal velocity and mass). This would represent an additional source of variability of the CE(U_w) resulting from different empirical models of the particle density, volume, and terminal velocity. The impact of more accurate particle tracking schemes on the total collection efficiency estimates is a matter of future work.

The numerical simulation of the CE(U_w) curve compares well with the real-world data and reveals that the two cases of wet and dry snow help explain the reason for the large variability in the in-field collection efficiency estimates. The numerically calculated CE from the LES runs for dry snow overestimated the reduction of CE with increasing U_w in the field data.

Acknowledgments. This research was supported through funding from the Ligurian District of Marine Technology and SITEP Italia (Italy), the National Center for Atmospheric Research (United States) NSF-funded Water System program, and the Natural Sciences and Engineering Research Council (NSERC) of Canada. Field data have been provided courtesy of Dr. Mareile Wolff and the Norwegian Meteorological Institute (http://met.no/English/).

REFERENCES

Colli, M., 2014: Assessing the accuracy of precipitation gauges: A CFD approach to model wind induced errors. Ph.D. thesis, School in Science and Technology for Engineering, University of Genova, 209 pp.

——, L. Lanza, R. Rasmussen, and J. M. Thériault, 2015a: The collection efficiency of shielded and unshielded precipitation gauges. Part I: CFD airflow modeling. *J. Hydrometeor.*, **17**, 231–243, doi:10.1175/JHM-D-15-0010.1.

——, R. Rasmussen, J. M. Thériault, L. Lanza, C. Baker, and J. Kochendorfer, 2015b: An improved trajectory model to evaluate the collection performance of snow gauges. *J. Appl. Meteor. Climatol.*, **54**, 1826–1836, doi:10.1175/JAMC-D-15-0035.1.

Folland, C., 1988: Numerical models of the raingauge exposure problem, field experiments and an improved collector design. *Quart. J. Roy. Meteor. Soc.*, **114**, 1485–1516, doi:10.1002/qj.49711448407.

Nešpor, V., 1995: Investigation of wind-induced error of precipitation measurements using a three-dimensional numerical simulation. Ph.D. thesis, Swiss Federal Institute of Technology Zurich, 109 pp.

——, and B. Sevruk, 1999: Estimation of wind-induced error of rainfall gauge measurements using a numerical simulation. *J. Atmos. Oceanic Technol.*, **16**, 450–464, doi:10.1175/1520-0426(1999)016<0450:EOWIEO>2.0.CO;2.

Rasmussen, R., J. Vivekanandan, J. Cole, B. Myers, and C. Masters, 1999: The estimation of snowfall rate using visibility. *J. Appl. Meteor.*, **38**, 1542–1563, doi:10.1175/1520-0450(1999)038<1542:TEOSRU>2.0.CO;2.

Stout, J. E., S. P. Arya, and E. L. Genikhovich, 1995: The effect of nonlinear drag on the motion and settling velocity of heavy particles. *J. Atmos. Sci.*, **52**, 3836–3848, doi:10.1175/1520-0469(1995)052<3836:TEONDO>2.0.CO;2.

Thériault, J., R. Rasmussen, K. Ikeda, and S. Landolt, 2012: Dependence of snow gauge collection efficiency on snowflake characteristics. *J. Appl. Meteor. Climatol.*, **51**, 745–762, doi:10.1175/JAMC-D-11-0116.1.

Wolff, M., K. Isaksen, A. Petersen-Øverleir, K. Ødemark, T. Reitan, and R. Bækkan, 2015: Derivation of a new continuous adjustment function for correcting wind-induced loss of solid precipitation: Results of a Norwegian field study. *Hydrol. Earth Syst. Sci.*, **19**, 951–967, doi:10.5194/hess-19-951-2015.

Yang, D., 2014: Double Fence Intercomparison Reference (DFIR) vs. Bush Gauge for true snowfall measurement. *J. Hydrol.*, **509**, 94–100, doi:10.1016/j.jhydrol.2013.08.052.

——, and Coauthors, 1999: Quantification of precipitation measurement discontinuity induced by wind shields on national gauges. *Water Resour. Res.*, **35**, 491–508, doi:10.1029/1998WR900042.